Journal of Solid State Chemistry **150,** 1–13 (2000)
doi:10.1006/jssc.1999.8539, available online at http://www.idealibrary.com on IDEAL®

Synthesis and Structure of a New Family of Nickelates: $Tl(Ln_2Sr_2)Ni_2O_9$, Ln = La, Pr, Nd, Sm, Eu, and Gd

C. S. Knee and M. T. Weller[1]

Department of Chemistry, The University of Southampton, Southampton, SO17 1BJ, United Kingdom

Received June 4, 1999; in revised form September 21, 1999; accepted October 22, 1999

A novel series of nickelates described by the formula $Tl(Ln_2Sr_2)Ni_2O_9$, Ln = La, Pr, Nd, Sm, Eu, and Gd, have been synthesized and their structures determined using both powder X-ray diffraction and powder neutron diffraction. The materials are isostructural with the superconducting cuprate, $Tl(La_{2.4}Ba_{1.6})Cu_2O_9$, crystallizing in a tetragonal unit cell, space group *I*4/*mmm*, lattice parameters $a = 3.8069–3.7667(1)$ Å and $c = 30.055–29.390(1)$ Å. The compounds adopt the 1201–0201 intergrowth structure, consisting of layers of apex-sharing stoichiometric NiO_6 octahedra connected by a TlO layer. A decrease in the cell dimensions is observed across the series, consistent with the lanthanide contraction and partial ordering of the strontium and lanthanide ions on the *A* cationic sites is observed. Magnetic susceptibility data reveal no evidence of long-range magnetic ordering for two of the compounds, $Tl(La_2Sr_2)Ni_2O_9$ and $Tl(Gd_2Sr_2)Ni_2O_9$. © 2000 Academic Press

Key Words: **powder X-ray diffraction; neutron diffraction; $Tl(La_{2+x}Ba_{2-x})Cu_2O_9$; 1201–0201 intergrowth; K_2NiF_4; layered nickelates.**

INTRODUCTION

The structural chemistry of complex nickelates has regained impetus from its relationship with that of cuprates, exhibiting high-temperature superconductivity. One area of particular interest has been complex nickel oxides adopting the perovskite and K_2NiF_4 structures which show magnetic and electrical similarities to the corresponding cuprates, e.g., $La_{2-x}Sr_xMO_{4\pm\delta}$ (M = Ni, Cu) (1, 2). Indeed, superconductivity has been claimed in lanthanum strontium nickelate but this has never been fully substantiated (3). A few other phases exist with structural analogies in copper and nickel chemistry, for example, Li_2MO_2 (4, 5) and "$BaMO_2$" (6, 7). These structural analogues derived from the ability of both copper(II) and nickel (II) to adopt four- (square planar), five- (square pyramidal), and six-fold (octahedron-based) coordinations to oxygen though the five- and six-fold geometries are usually more distorted for copper due to the Jahn–Teller effect. More recently, the synthesis of $TlSr_2NiO_{4+\delta}$ (8), a nickel analogue of the end member of a high T_c cuprate family, $TlSr_2CuO_y$, further demonstrated the ability of nickelates to adopt similar structures to cuprates. In fact, the two phases exhibit a remarkable degree of structural correlation, with ordering of oxygen vacancies occurring along the *b* direction, resulting in a 2*b* supercell for both compounds (9, 10). The synthesis of $TlSr_2CuO_y$ was achieved after the isolation of cation-substituted 1201 phases such as $TlSr_{2-x}Ln_xCuO_y$, Ln = La or Nd and $x = 0.5–1.0$, which exhibit transition temperatures as high as 48 K (11). The introduction of trivalent cations stabilizes the 1201 structure for copper and gives rise to complete CuO_2 basal layers required for superconductivity.

In this paper we report the results of an investigation into lanthanide substitution within the Tl–Sr–Ni–O system. This led to the isolation of a new series of nickel oxide materials, $Tl(Ln_2Sr_2)Ni_2O_9$, Ln = La (12), Pr, Nd, Sm, Eu, and Gd. The compounds adopt the 1201–0201 intergrowth structure first determined for the superconducting phase $Tl(La_{2.4}Ba_{1.6})Cu_2O_9$, T_c = 35 K (13), consisting of the 1201 ($TlSr_2CuO_5$) and 0201 (La_2CuO_4) structures. Structural characterization of the materials has been performed using Rietveld analysis of both powder X-ray diffraction (PXD) and powder neutron diffraction (PND) data, and the magnetic behavior of two representative samples has been determined. Structural trends that are apparent for the series of compounds are discussed, and comparisons with related materials are made.

EXPERIMENTAL

The synthesis of a series of compounds of the stoichiometry $Tl(Ln_2Sr_2)Ni_2O_9$ was performed via the reaction of Tl_2O_3, Ln_2O_3 (Ln = La, Nd, Sm, Eu, Gd, Dy, and Er), Pr_6O_{11} or Tb_4O_7, and $Sr_2Ni_2O_5$ synthesized following the literature method (14). The lanthanide oxides were heated to 1000°C in air prior to weighing to decompose any carbonate material to oxide. The reactants were ground

[1]To whom correspondence should be addressed. Fax: 00 44 1703 593592. E-mail: mtw@soton.ac.uk.

0022-4596/00 $35.00

TABLE 1
Synthetic Conditions Employed and the Results Obtained in the Investigation of the Series $Tl(Ln_2Sr_2)Ni_2O_9$, Ln = La to Er

Target phase	Conditions		Product
	Temp. (°C)	Duration (h)	
$Tl(La_2Sr_2)Ni_2O_9$	900	5	$Tl(La_2Sr_2)Ni_2O_9$
$Tl(Pr_2Sr_2)Ni_2O_9$	900	5	$Tl(Pr_2Sr_2)Ni_2O_9$
$Tl(Nd_2Sr_2)Ni_2O_9$	900	5	$Tl(Nd_2Sr_2)Ni_2O_9$
$Tl(Sm_2Sr_2)Ni_2O_9$	900	10	$Tl(Sm_2Sr_2)Ni_2O_9$
$Tl(Eu_2Sr_2)Ni_2O_9$	900	10	$Tl(Eu_2Sr_2)Ni_2O_9$
$Tl(Gd_2Sr_2)Ni_2O_9$	900	10	$Tl(Gd_2Sr_2)Ni_2O_9$
$Tl(Tb_2Sr_2)Ni_2O_9$	900–950	5–20	$Tl_2Sr_4O_7$, Tb_2SrO_4, NiO
$Tl(Dy_2Sr_2)Ni_2O_9$	900–950	5–20	$Tl_2Sr_4O_7$, Dy_2SrO_4, NiO
$Tl(Er_2Sr_2)Ni_2O_9$	900–950	5–20	$Tl_2Sr_4O_7$, Er_2SrO_4, NiO

thoroughly, pressed into 13-mm diameter pellets under $\sim$10 tons/cm^2 and sealed inside a gold tube by crimping the ends. The capsule was then slowly ramped to 900°C, fired for 5–10 h, and then allowed to furnace cool. Variation of the initial thallium content resulted in the starting metal ratio 0.8Tl : 1Ln : 1Sr : 1Ni being adopted to provide samples of the highest purity. The resulting powders were examined using a Siemens D5000 diffractometer (Cu$K\alpha_1$ radiation). The results obtained for the range of lanthanides are summarized in Table 1.

Phase Formation

The synthesis of a Ce derivative was not attempted, due to the stability and ready formation of Ce(IV). A firing time of 5 h for all the lanthanides listed in the Experimental section was initially employed. This produced black, monophasic samples of $Tl(Ln_2Sr_2)Ni_2O_9$, with Ln = La, Pr, and Nd. A further 5-h sintering period was found to be necessary for the smaller lanthanides, Sm, Eu, and Gd, to completely remove the impurity phase $Tl_2Sr_4O_7$. The products obtained from the synthesis of the Tb, Dy, and Er experiments were yellow, indicating the presence of some $Tl_2Sr_4O_7$ which was confirmed by PXD analysis. These samples also contained Ln_2SrO_4 (15) and NiO and no reflections characteristic of the 1201–0201 phase were observed.

Higher temperatures and longer sintering periods were undertaken but no sample with the target phases present could be obtained. The decreasing size of the lanthanide is believed to be responsible for the observed phase behavior, with the large- and medium-sized lanthanides (La to Gd) forming the 1201–0201 intergrowth structure before a transition at Tb occurs and the Ln_2SrO_4 phase becomes stable. Similar behavior is observed for the synthesis of the related Ln_2NiO_4 phases, with the K_2NiF_4-type structure being adopted for Ln = La, Pr, and Nd, before a shift in relative stability occurs, which prevents the synthesis of Sm_2NiO_4 and the other smaller rare earth Ln_2NiO_4 phases. A probable reason for this transition is the size incompatibility of the basal Ni–O bonds and the smaller Sm–O layer and it is likely that similar factors are responsible for the inability to isolate $Tl(Ln_2Sr_2)Ni_2O_9$ with lanthanides smaller than Gd.

The starting mixtures contained a 60% excess of thallium, with respect to the other metals. This was necessary to counteract the observed thallium loss from the gold capsules during synthesis. The mass loss during reaction was monitored and found to be consistent with the target stoichiometry $Tl(Ln_2Sr_2)Ni_2O_9$, assuming the only mechanism for mass loss was the escape of Tl_2O(g) at elevated temperature.

STRUCTURE DETERMINATION

Powder X-Ray Diffraction Data

Data from the six samples of the series $Tl(Ln_2Sr_2)Ni_2O_9$, Ln = La, Pr, Nd, Sm, Eu, and Gd, were indexed with a body-centered (reflection condition $h + k + l = 2n$) tetragonal unit cell, $a \approx 3.8$ and $c \approx 30.0$ Å. Cell parameters were refined using the CELL program before further structural analysis was performed by Rietveld refinement using the GSAS program (16). Data were collected in the 2θ range 17°–117° over a 17-h period with a step size of 0.02°. The starting structural model was taken from that of $Tl(Ba_2La_2)Cu_2O_9$ (13), in the space group $I4/mmm$ with thallium on (0, 0, 0), nickel on (0, 0, z) $z \approx 0.15$, mixed Ln/Sr sites at (0.5, 0.5, z) $z \approx 0.08$, Ln/Sr(1), and (0.5, 0.5, z) $z \approx 0.2$, Ln/Sr(1). Oxygen atoms were located on (0.5, 0.5, 0). O(1); (0, 0, z) $z \approx 0.07$, O(2); (0.5, 0, z) $z \approx 0.15$, O(3), and (0, 0, z) $z \approx 0.2$, O(4). The Ln/Sr site occupancies were set at 50:50 in the initial stages of the refinements.

Structure Refinement of $Tl(La_2Sr_2)Ni_2O_9$—PXD Data

Preliminary stages of the refinement placed all atoms on the special sites at full occupancy and proceeded with the variation of global parameters such as background and peak profile coefficients and the lattice constants. The isotropic temperature factors for the individual atoms were then introduced and along with the refinement of atomic positions, resulted in the expected improvement in the least-squares fit. The temperature factor for the thallium atom refined to an unrealistically large value and this atom was therefore placed on a new 4-fold site (x, y, 0) at quarter occupancy. This displacement refined steadily with $x = y \approx 0.05$ and a simultaneous reduction in the thermal parameter to an acceptable value. Attention was then focused on the mixed La/Sr sites, in particular, the La/Sr(2) (0.5, 0.5, 0.2) site which had an unreasonably low temperature factor. The temperature factors of the two atoms on

the site were constrained to the same value, and then the fractional occupancy of the site was reciprocally linked and allowed to vary from the initial 50:50 ratio. The site was found to favor a marked increase in the La content to $\sim$0.7 and the thermal parameter now refined to a larger, more sensible value. The occupancy of the La/Sr(1) site was probed in this way and was found to favor a decrease in La content to $\sim$ 0.35. Attempts were then made to refine the occupancies of the two mixed sites simultaneously without constraining the overall La and Sr content. This, however, produced large fluctuations in the fractional occupancies. Therefore, the temperature factors of the four atoms were linked and constrained to the same value. In addition, the occupancies of the atoms on an individual site were linked to produce a total occupancy of unity and the values on the two sites constrained to give a total occupation of 2La and 2Sr, consistent with the initial reactant mixture. On variation of the atomic parameters, this arrangement produced stable refinements and resulted in a decrease in the La content on the La/Sr(1) site compensated by an increase on the La/Sr(2) position. A sensible thermal parameter for the two sites was also obtained. The temperature factors of the oxygen atoms all refined to acceptable values and no attempts to probe their occupancies were made.

A similar refinement process was followed for the five other data sets. All the materials favored a disordering of the thallium site and large variations in the occupancies of the mixed Ln/Sr sites were also observed. The two Ln/Sr sites were initially not linked; instead, the occupancies of the individual sites were varied independently. This resulted in a decrease of the lanthanide on the Ln/Sr(1) site and a concomitant increase in lanthanide occupation of the Ln/Sr(2) position for all the compounds, e.g., the refined occupancies obtained for the Pr and Eu refinements were 0.38/0.62(3) and 0.19/0.81(3) for the Ln/Sr(1) site and 0.67/0.43(4) and 0.78/0.22(4) for the Ln/Sr(2) site. Crystallographic data for all six phases are summarized in Table 2, and the profile fit obtained for $Tl(Eu_2Sr_2)Ni_2O_9$ is shown in Fig. 1. Note: the R_p and R_{wp} fit parameters obtained for the PXD refinements (Table 3) are all artificially high due to the inability to accurately fit the low background obtained in the data sets.

Discussion of PXD Refinements

The basic structure of the $Tl(Ln_2Sr_2)Ni_2O_9$ phases is shown in Fig. 2. It is made up of a section consisting of two NiO_6 perovskite blocks separated by a TlO_6 octahedra rotated through 45°. This 1201-type unit is displaced by $a/2$ and repeated, leading to the observed body centering. This behavior is reminiscent of that observed for the Ruddlesden–Popper phase $Sr_4Ti_3O_7$ (17). The cell parameters obtained for the series show the expected decrease in size on

TABLE 2
Structural Parameters Refined from PXD Data (Temperature Factor *B* (in Å^2), *n* the Site Occupancy, and Cell Parameters (in Å) Are Also Shown; Space Group *I*4/*mmm*

Atom	TlSrLaNi	TlSrPrNi	TlSrNdNi	TlSrSmNi	TlSrEuNi	TlSrGdNi
Tl: (*x*)	0.054(2)	0.046(3)	0.054(2)	0.035(3)	0.052(2)	0.048(3)
B	1.3(2)	2.0(2)	1.1(2)	2.5(2)	1.3(2)	1.2(2)
Ln/Sr(1): (*z*)	0.0850(1)	0.0854(1)	0.0857(1)	0.0858(2)	0.0861(2)	0.0861(2)
B	1.24(6)	1.40(6)	1.13(5)	1.28(6)	1.44(6)	1.18(7)
n	0.32/0.68(1)	0.26/0.74(1)	0.25/0.75(1)	0.20/0.80(1)	0.19/0.81(1)	0.18/0.82(1)
Ln/Sr(2): (*z*)	0.2033(1)	0.2038(1)	0.2040(1)	0.2041(1)	0.2037(1)	0.2038(1)
B	1.24(6)	1.40(6)	1.13(5)	1.28(6)	1.44(6)	1.18(7)
n	0.68/0.32(1)	0.74/0.26(1)	0.75/0.35(1)	0.80/0.20(1)	0.81/0.19(1)	0.82/0.18(1)
Ni: (*z*)	0.1459(3)	0.1471(4)	0.1461(3)	0.1479(4)	0.1490(4)	0.1475(4)
B	1.49(15)	1.67(16)	1.52(15)	1.56(16)	1.45(15)	1.69(17)
O(1): *B*	3.9(2)	6.0(2)	6.3(2)	3.9(2)	6.0(2)	8.1(6)
O(2): (*z*)	0.0716(8)	0.0721(11)	0.0704(9)	0.0737(14)	0.0714(12)	0.0703(16)
B	3.0(1)	4.0(1)	1.9(1)	5.9(2)	5.1(1)	7.1(2)
O(3): (*z*)	0.1440(7)	0.1435(7)	0.1425(7)	0.1451(9)	0.1467(8)	0.1473(9)
B	1.9(5)	2.2(5)	2.4(5)	2.7(5)	2.5(5)	1.1(5)
O(4): (*z*)	0.2170(9)	0.2172(9)	0.2182(10)	0.2216(10)	0.2216(10)	0.2208(10)
B	2.2(9)	1.7(8)	2.0(8)	2.1(8)	2.4(8)	0.8(1)
a	3.8069(1)	3.7864(1)	3.7794(1)	3.7718(1)	3.7711(1)	3.7667(1)
c	30.055(1)	29.804(1)	29.697(1)	29.524(1)	29.421(1)	29.390(1)

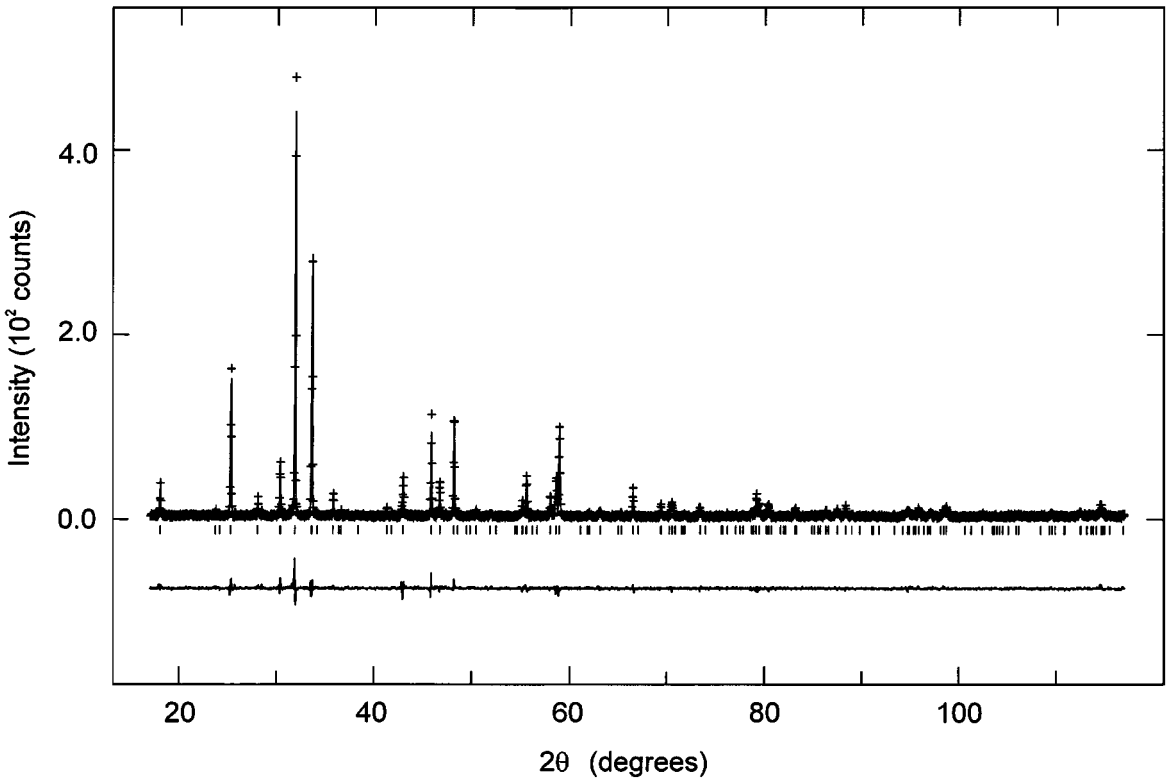

FIG. 1. Final fit achieved to the $Tl(Eu_2Sr_2)Ni_2O_9$ PXD data in the 2θ range 17°–117°. Crosses mark observed intensities, upper continuous line the calculated profile, and the lower line the difference. Tick marks show allowed reflections for $Tl(Eu_2Sr_2)Ni_2O_9$.

crossing the lanthanide series from La to Gd (Fig. 3). The *c* parameter shows a 0.66 Å reduction and the *a* parameter a 0.04 Å decrease, corresponding to a 3.2% contraction of the unit cell volume. Examination of the different structural portions of the materials reveals that the contraction of the *c* parameter is a result of two factors: shrinkage of the apical Tl–O(2) distance by ($\sim$0.14 Å) from the La material to the Gd-containing phase, and a similar decrease in the Ln/Sr(2)–O(4) apical bond. The Ni–O(2) and Ni–O(4) apical distances show no discernible downward trend; indeed, those determined for $Tl(Gd_2Sr_2)Ni_2O_9$ are actually the largest in the series (Table 3). A contraction of the *a* parameter is also observed across the series, with both the Tl–O(1) distances and the basal Ni–O(3) distances reflecting the decrease. The driving force for the observed contraction is the introduction of successively smaller lanthanides onto the *A* site of the structure. The ionic radius radius of La^{3+} in 9-fold coordination is 1.216 Å compared to 1.107 Å for Gd^{3+} (18). The results suggest that the presence of La places the structure under expansive stress and this is relieved by the substitution of smaller lanthanides. A shift in phase behavior occurs upon the introduction of Tb^{3+} (i.r. = 1.095 Å) and Dy^{3+} (i.r. = 1.083 Å) into the structure, and the 1201–0201 structure is no longer stable. The mismatch between the perovskite Ni–O and rock salt Ln–O layers becomes too great, and $Tl_2Sr_4O_7$, NiO, and Ln_2SrO_4 form. The formation of phases with rare earths as small as Tb and Dy in 9-fold coordinations is unusual; lower coordinations are usually favored like the 6-fold sites found in Tb_2SrO_4 and Dy_2SrO_4 (15).

Cation Ordering

An important factor in the six refinements was the variation of the occupancy of the mixed *Ln*/Sr sites. This led to large improvements in the profile fits and has important consequences regarding the structure of the materials. Table 4 summarizes the results obtained from the structural analyses. The results reveal that partial ordering of the lanthanide and strontium ions occurs for all the compounds, with the *Ln*Sr(2) position favoring an increase in the smaller lanthanide. As the size mismatch, defined by $(r_{sr} - r_{Ln})/r_{Ln} \times 100$, between Sr and the lanthanide increases from $\sim$8% for La to $\sim$18% for Gd, then a trend to greater segregation on the site is also observed. Examination of Table 3 reveals that a marked contraction of the bond lengths around the Ln/Sr(2) site occurs as the lanthanide series is crossed; e.g., the Ln/Sr(2)–O(4) apical bond

TABLE 3
Interatomic Distances (in Å) Determined from PXD Data (e.s.d.'s Are Given in Parentheses; Final Fit Parameters Are Also Shown)

	$Tl(Ln_2Sr_2)Ni_2O_9$					
Bond	La	Pr	Nd	Sm	Eu	Gd
Tl–O(1) × 2	2.708(1)	2.689(1)	2.688(1)	2.674(1)	2.681(1)	2.676(1)
Tl–O(1) × 2	2.985(11)	2.923(15)	2.961(10)	2.854(17)	2.941(12)	2.918(15)
Tl–O(2) × 2	2.17(3)	2.16(3)	2.11(3)	2.18(4)	2.12(4)	2.08(5)
Ln(1)–O(1) × 1	2.553(4)	2.546(4)	2.546(4)	2.532(5)	2.533(5)	2.532(5)
Ln(1)–O(2) × 4	2.721(4)	2.706(5)	2.711(5)	2.691(6)	2.701(6)	2.704(8)
Ln(1)–O(3) × 4	2.602(14)	2.565(15)	2.533(15)	2.574(18)	2.596(17)	2.604(19)
Ln(2)–O(3) × 4	2.608(14)	2.611(15)	2.628(16)	2.567(17)	2.523(16)	2.511(18)
Ln(2)–O(4) × 4	2.723(4)	2.707(4)	2.705(5)	2.717(6)	2.718(6)	2.710(5)
Ln(2)–O(4) × 1	2.40(3)	2.36(3)	2.31(3)	2.19(3)	2.19(3)	2.21(3)
Ni–O(3) × 4	1.904(1)	1.896(1)	1.893(1)	1.887(1)	1.887(1)	1.883(1)
Ni–O(2) × 1	2.23(3)	2.23(4)	2.25(3)	2.19(4)	2.28(4)	2.30(5)
Ni–O(4) × 1	2.14(2)	2.09(3)	2.14(3)	2.17(3)	2.14(3)	2.14(3)
R_B (%)	8.80	10.91	10.55	11.32	11.01	11.28
R_p (%)	17.1	17.0	16.6	16.0	15.4	14.5
R_{wp} (%)	23.2	23.3	22.9	21.6	20.6	18.9
χ^2	1.35	1.57	1.54	1.37	1.35	1.24

decreases by 0.2 Å and the Ln/Sr(2)–O(3) distances drops by 0.1 Å. This compares with the *Ln*/Sr(1)–oxygen bond lengths which remain virtually constant, implying that the oxygen ions are unable to relax around the Ln/Sr(1) site of the 1201–0201 phases. Instead, contraction occurs at the *Ln*/Sr(2) site, which corresponds to shrinkage in the interlayer separation between the 1201-type blocks.

The ordering of lanthanide and strontium ions on the *A* (or K)-type sites of the 1201–0201 materials is an important feature of the structure, particularly as the related K_2NiF_4 phases, i.e., $Ln_{2-x}Sr_xNiO_4$, *Ln* = La (2), Pr, Sm, Gd (19–21), and Nd (22), display a random cationic distribution. There is, however, evidence of local adjustments of the K-type site in the defect K_2NiF_4 phase, $YSr_5Ni_3O_{11}$ (23) where the disparity in ionic radii is even greater. Forcing both cations to support 9-fold coordinations within the 1201–0201 structure results in the observed segregation of the *A* sites. As the lanthanide ion becomes smaller, the *Ln*/Sr(1) position becomes increasingly less suitable to accommodate the atom, and greater cationic separation occurs.

The thallium coordination of the six compounds exhibits disorder of the thallium atom which is moved off the ideal 2*a* (0, 0, 0) site onto a 4-fold 8*h* (*x*, *y*, 0) $x \approx y \approx 0.05$ site. The origin of this disorder is a need to minimize the bond mismatch between the rock salt TlO layer and the larger perovskite NiO_2 layers above and below. Given that the 0201–1201 structure is so closely related to the $TlSr_2MO_5$ (*M* = Cu, Ni) 1201 structure, it is not surprising that the $Tl(Ln_2Sr_2)Ni_2O_9$ family also reveals this structural feature which is common for all single-layer thallium–oxygen materials (24, 25). Indeed, other "intergrowth" materials, e.g., $TlSr_4Fe_2O_9$ (26) display similar ($x = 0.08$) displacements.

The nickel coordination of the $Tl(Ln_2Sr_2)Ni_2O_9$ phases consists of an elongated NiO_6 octahedron with in-plane distances ranging from 1.904(1) Å for the La phase to 1.883(1) Å for the Gd compound (Fig. 4). These units are linked, by sharing apices, to form infinite layers in the *ab* plane of stoichiometry NiO_2. PXD data reveal no evidence of oxygen vacancies in these planes, in contrast to the related 1201 phase $TlSr_2NiO_{4+\delta}$ (9). Assuming that all thallium is present as Tl(III) and full occupation of the oxide ion sites, nickel will be present in a formal valence of $Ni^{2.5+}$, i.e., an equal fraction of Ni^{2+} and Ni^{3+} in the 1201–0201 materials. This compares with a formal Ni oxidation state of ~2.7, determined from PND data, in $TlSr_2NiO_{4+\delta}$. The

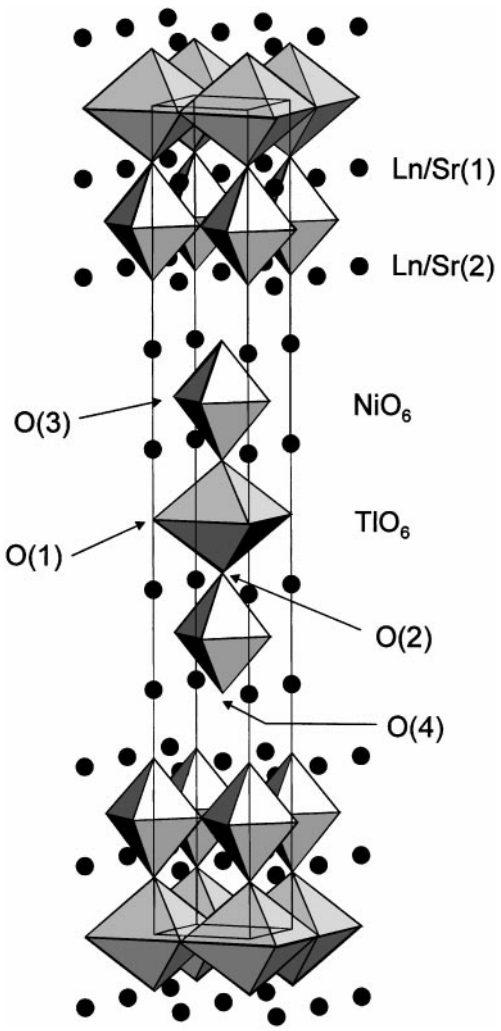

FIG. 2. Idealized structure of $Tl(Ln_2Sr_2)Ni_2O_9$. The thallium and nickel coordinations are shown as octahedra, dark spheres represent the mixed Ln/Sr sites, and oxygen positions are labeled.

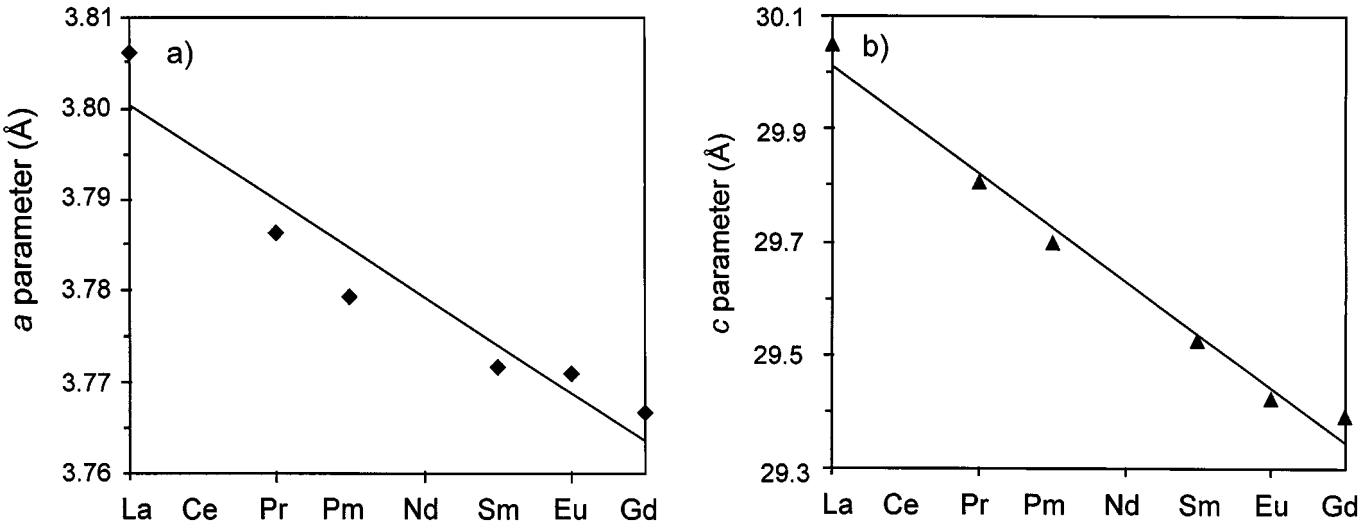

FIG. 3. Variation in the lattice constants determined for the series $Tl(Ln_2Sr_2)Ni_2O_9$, Ln = La, Pr, Nd, Sm, Eu, and Gd. Contraction of the a parameter is shown in Fig. 3a, and the decrease in the c parameter is shown Fig. 3b.

presence of Ni^{3+} suggests Jahn–Teller effects are responsible for the elongation of the NiO_6 octahedra. This, however, does not explain the fact that there are two distinct apical Ni–O distances, the longer Ni–O(2) bonds ($\sim$2.25 Å) and the shorter Ni–O(4) interactions ($\sim$2.14 Å). These different apical Ni–O bonds are believed to be caused by the cationic segregation producing different types of rock salt layers, i.e., LnO and SrO above and below the perovskite Ni–O layers. Another feature is that the NiO_2 planes are buckled, with the O(3) oxygen atoms lying $\sim$0.1 Å above/below the nickel atom. The exception to this is $Tl(Gd_2Sr_2)Ni_2O_9$ which has flat NiO_2 layers, i.e., Ni(z) = 0.1475(4) and O(3): (z) = 0.1473(9). The puckering of the planes suggests a compressive strain on the planar Ni–O environment, which is relieved by the vertical displacement of the oxygen atoms relative to the central nickel. However, this is not consistent with the anomalous flat planes observed for the material containing Gd, the smallest lanthanide for which the structure is stable. Therefore, it is suggested that the different makeup of the layers surrounding the NiO_6 octahedra in the $Tl(Ln_2Sr_2)Ni_2O_9$ materials is also responsible for the buckling distortion.

TABLE 4
***Ln*/Sr Occupancies Determined from PXD**

	$Tl(Ln_2Sr_2)Ni_2O_9$					
Site	La	Pr	Nd	Sm	Eu	Gd
Ln/Sr(1)	0.32/0.68(1)	0.26/0.74(1)	0.25/0.75(1)	0.20/0.80(1)	0.19/0.81(1)	0.18/0.82(1)
Ln/Sr(2)	0.68/0.32(1)	0.74/0.26(1)	0.75/0.25(1)	0.80/0.20(1)	0.81/0.19(1)	0.82/0.18(1)

More definite conclusions concerning the exact Ni–O environment, and other features linked to the oxygen sublattice, required powder neutron diffraction analysis.

POWDER NEUTRON DIFFRACTION (PND) DATA

Data Collection

PND data were collected for the $Tl(Ln_2Sr_2)Ni_2O_9$, Ln = La, Pr, Nd, and ^{154}Sm, materials at room temperature

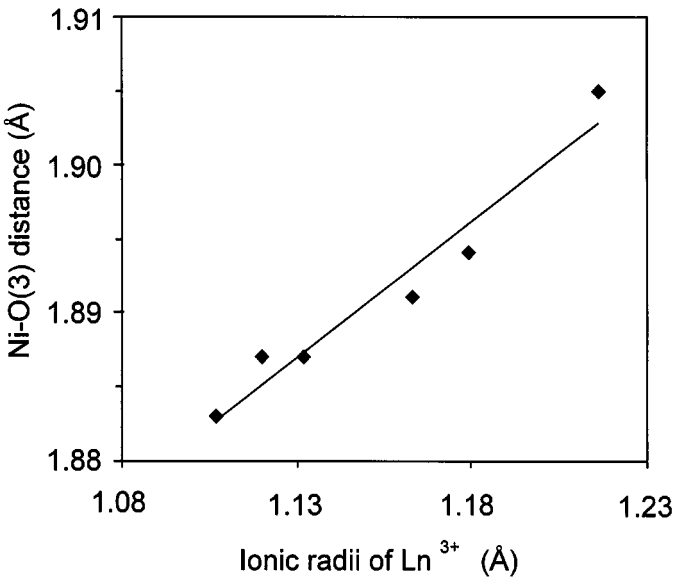

FIG. 4. The Ni–O basal distance (in Å) versus lanthanide ionic radii for the $Tl(Ln_2Sr_2)Ni_2O_9$ series.

on the POLARIS diffractometer at the ISIS facility, Oxfordshire, U.K. Approximately 2 g of material was placed into a 9-mm diameter vanadium and the powder pattern collected for a duration of 5 h using the back-scattering detector bank. The use of an isotopically substituted Sm sample is necessary due to the high absorption of the more abundant ^{149}Sm nucleus. Then, 5-K data were collected on the $Tl(Ln_2Sr_2)Ni_2O_9$, Ln = La, Pr, and Nd, samples using the constant wavelength ($\lambda = 1.911$ Å) diffractometer D1A at the I.L.L., Grenoble, France. The samples were placed into a 6-mm diameter vanadium can and cooled to 5 K in a standard I.L.L. cryostat. The powder pattern was collected at steps of $2\theta = 0.05^\circ$ over the range 0°–160° over a time period of 8 h. The PND patterns were refined using the structural model determined from PXD data as the starting point. The nuclear scattering lengths were taken to be Tl = 8.878, Sr = 7.020, La = 8.240, Pr = 4.580, Nd = 7.690, ^{154}Sm = 8.0, Ni = 10.030, and O = 5.805 fm (27). Introduction of global parameters, e.g., background and profile coefficients, proceeded smoothly. The presence of a small level of NiO impurity (< 5%) in all data sets was apparent and this was fitted using literature data and variation of the cell constant and phase fraction.

Structure Refinement—PND Data

Refinement of both room temperature and 5-K data proceeded in a similar fashion to that described for the PXD data. Disorder in the Tl–O(1) plane was modeled by displacing both the Tl atom and the O(1) atom onto 4-fold sites. This reduced the rather high temperature factors associated with both atoms. In fact, modeling the disorder led to unphysical, negative values for the thermal parameter of the thallium atom in the 5 K refinements. The occupancies of the mixed Ln/Sr sites were linked in the same rigorous manner as that used for the PXD analysis. It was recognized that the contrast in scattering lengths between the lanthanide and strontium ions was not large for the majority of the refinements, e.g., $b_{Sr} = 7.02$ and $b_{La} = 8.24$ fm. However, this arrangement produced a stable refinement, fractional occupancies in line with those obtained in the PXD refinements and satisfactory temperature factors (for the room temperature data). The thermal parameters obtained for the 5-K analyses were lower than expected; indeed, the value associated with the mixed Nd/Sr sites was negative. The positional coordinates and thermal parameters of the oxygen atoms all refined satisfactorily, and no evidence of oxygen vacancies was found. Initially the Ln/Sr sites of the

TABLE 5
Structural Parameters Refined from PND Data (Temperature Factor B (in Å^2), n the Site Occupancy; Cell Parameters (in Å); Space Group *I4/mmm*; * Indicates 5-K Data)

	$Tl(Ln_2Sr_2)Ni_2O_9$						
Atom	La	La*	Pr	Pr*	Nd	Nd*	Sm
Tl: (x)	0.0363(10)	0.0467(15)	0.0392(9)	0.0456(14)	0.0358(10)	0.0441(15)	0.0380(12)
B	0.95(6)	− 0.24(12)	0.79(7)	− 0.30(12)	0.69(7)	− 0.28(12)	0.23(9)
Ln/Sr(1): (z)	0.08439(5)	0.08417(9)	0.08486(6)	0.08430(10)	0.08515(6)	0.08457(9)	0.08546(9)
B	0.25(2)	0.17(3)	0.27(2)	0.03(3)	0.23(2)	− 0.05(3)	0.24(3)
n	0.35/0.65(2)	0.34/0.66(3)	0.33/0.67(1)	0.29/0.71(1)	0.20/0.80(5)	0.15/0.85(5)	0.30/0.70(7)
Ln/Sr(2): (z)	0.20321(4)	0.20355(7)	0.20404(6)	0.20421(10)	0.20355(5)	0.20370(7)	0.20379(8)
B	0.25(2)	0.17(3)	0.27(2)	0.03(3)	0.23(2)	− 0.05(3)	0.24(3)
n	0.65/0.25(2)	0.66/0.34	0.67/0.33(1)	0.71/0.29(1)	0.80/0.20(5)	0.85/0.15(5)	0.70/0.30(7)
Ni: (z)	0.14719(4)	0.14674(6)	0.14759(4)	0.14752(6)	0.14753(5)	0.14735(7)	0.14807(10)
B	0.19(2)	0.22(3)	0.29(2)	0.24(4)	0.23(1)	0.33(3)	0.32(3)
O(1): (x)	0.551(1)	0.544(2)	0.553(1)	0.544(2)	0.550(1)	0.544(3)	0.562(2)
B	0.63(8)	1.38(22)	1.1(10)	1.34(25)	0.87(11)	1.34(26)	1.8(3)
O(2): (z)	0.06924(8)	0.06882(11)	0.06977(9)	0.06954(12)	0.07025(10)	0.06983(11)	0.07061(17)
B	1.30(4)	1.04(6)	1.45(4)	0.95(7)	1.46(4)	1.25(7)	1.22(8)
O(3): (z)	0.14387(5)	0.14389(11)	0.14478(6)	0.14527(10)	0.14519(7)	0.14569(10)	0.14761(15)
B	0.43(1)	0.44(3)	0.55(1)	0.38(3)	0.56(2)	0.50(4)	0.71(3)
O(4): (z)	0.21708(8)	0.21681(12)	0.21797(9)	0.21781(12)	0.21829(10)	0.21797(10)	0.21831(20)
B	0.82(3)	0.80(6)	0.99(3)	0.85(7)	1.05(3)	0.86(6)	1.52(6)
a	3.8084(1)	3.7993(1)	3.7890(1)	3.7791(1)	3.7810(1)	3.7732(1)	3.7780(1)
c	30.0748(5)	29.9587(6)	29.8283(7)	29.7035(6)	29.7123(7)	29.5909(6)	29.6939(13)

praseodymium refinements were not linked; instead, the occupancies of the individual sites were varied independently. The contrast between the scattering lengths of Sr and Pr is large, i.e., $b_{Sr} = 7.02$ fm and $b_{Pr} = 4.58$ fm. This resulted in the expected decrease of Pr on the *Ln*/Sr(1) site and a concomitant increase in the praseodymium occupation of the *Ln*/Sr(2) position for both the ambient- and low-temperature data. The refined occupancies were consistent with the constrained PXD refinement; for example, the values determined from the POLARIS data were 0.26/0.74(2) for the Pr/Sr(1) site and 0.78/0.22(2) for the Pr/Sr(2) position, compared to 0.26/0.74(1) and 0.74/0.26(1) determined from PXD. The sites were linked in later cycles of the Pr refinement for consistency. The refined atomic coordinates are summarized in Table 5. The final profile fit to the $Tl(Nd_2Sr_2)Ni_2O_9$ (room-temperature data) is shown in Fig. 5 and the fit to the $Tl(La_2Sr_2)Ni_2O_9$ (5-K data) shown in Fig. 6.

Discussion of PND Refinements

Analysis of neutron data has allowed a number of structural subtleties linked to the oxygen ions to be accurately resolved. These include displacement of the O(1) atom in the Tl–O layer, and accurate determination of both the degree of "buckling" in the NiO_2 planes and the oxygen content of the compounds. The origins of the disorder present in the Tl–O plane have been discussed above; however, the PXD analysis did not permit the splitting of the 2*b* (0.5, 0.5, 0) O(1) site onto a 4-fold 8*h* (*x*, *y*, 0) $x \approx y \approx 0.55$ position. This displacement of the Tl and O(1) atoms correspond to approximate shifts of 0.15 and 0.2 Å in the *xy* plane, respectively, reflecting the strain caused by the imperfect match of the two types of layers. No evidence of a superstructure due to the displacements being correlated was found and the TlO coordination is best described, on average, as distorted octahedral.

The degree of puckering of the NiO_2 planes, as evidenced by the O(3)–Ni–O(3) bond angle (see Fig. 7 and 8), has been more accurately determined and is shown in Table 6 along with relevant interatomic distances. The results show a decrease in the level of buckling as the lanthanide ion decreases in size for both the room-temperature and 5-K data. This is in agreement with the observation of flat NiO_2 planes for $Tl(Gd_2Sr_2)Ni_2O_9$ from the PXD data (Table 2). The PND results confirm the hypothesis that the buckling of the planes results from the bonding requirements of the surrounding *Ln* and SrO network rather than the effects of compressive strain on the Ni–O(3) basal bond. The axial Ni–O(2)/O(4) bond distances show a small downward trend,

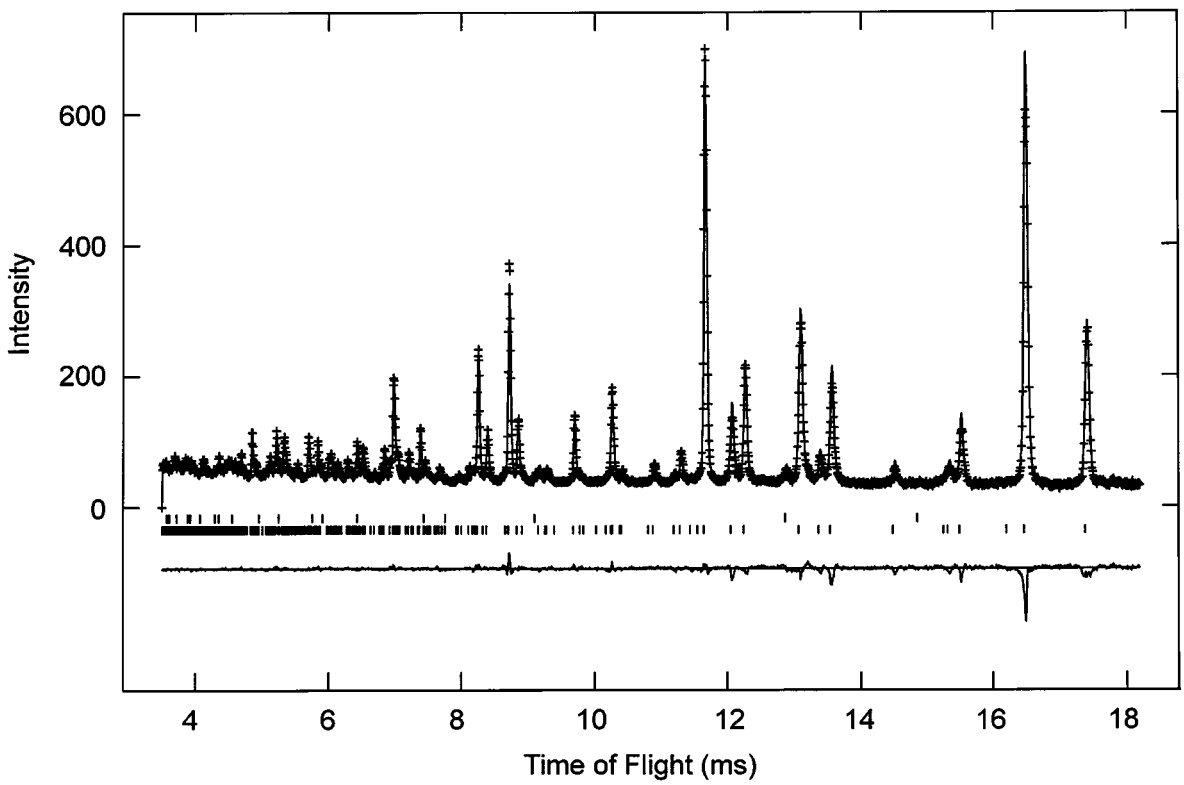

FIG. 5. Final fit achieved to the room temperature, time of flight, PND data of $Tl(Nd_2Sr_2)Ni_2O_9$. Crosses mark observed intensities, upper continuous line the calculated profile, and the lower line the difference. Tick marks show allowed reflections for $Tl(Nd_2Sr_2)Ni_2O_9$.

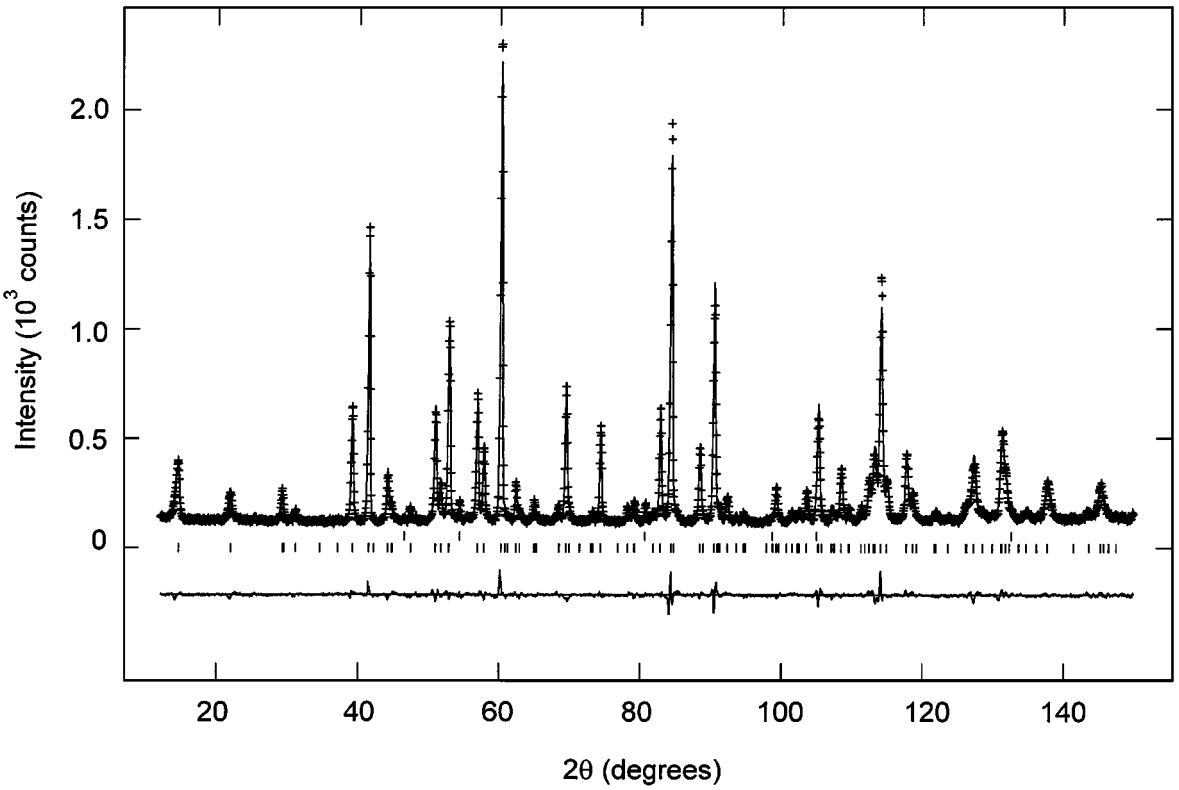

FIG. 6. Final fit achieved to the 5 K, constant wavelength, PND data of $Tl(La_2Sr_2)Ni_2O_9$. Crosses mark observed intensities, upper continuous line the calculated profile, and the lower line the difference. Tick marks show allowed reflections for $Tl(La_2Sr_2)Ni_2O_9$.

particularly the Ni–O(2) interaction, as the lanthanide ion becomes smaller (Fig. 8). This is somewhat different from the PXD refinements which showed no apparent trend for these distances (Table 3). The oxygen content of the four materials was probed to check for any vacancies; however, refinement of the site occupancies produced only negligible deviations from full occupation. The nickel oxidation state of the materials was therefore confirmed as $+2.5$.

The low-temperature data reveal the expected contraction of cell constants (and consequently bond lengths) with the a parameter shrinking by ~ 0.01 Å and the c parameter by ~ 0.12 Å. The contraction occurs uniformly with no particular section of the structure displaying a pronounced reduction in apical distances. The most significant result obtained from the 5-K data is the observation of negative temperature factors for the displaced thallium atom. The data confirm that the disorder is structural rather than thermal. The value of the displacement within the xy plane is actually greater for the low-temperature data than that observed for the room-temperature scans (Table 5). The lower than expected thermal parameters obtained for the mixed Ln/Sr sites, and the large standard deviations associated with them, possibly reflect local adjustments of the structure around the cationic sites. This is to be expected given that the difference in size of the cations is large and cationic segregation on the two sites is incomplete.

COMPARISON WITH $Ln_{2-x}Sr_xNiO_4$ MATERIALS

Much of the recent interest in the $Ln_{2-x}Sr_x$ NiO_4 (Ln = La, Pr, Nd, Sm, Eu, and Gd) phases has been generated from the similarities in the materials to the superconducting K_2NiF_4 materials such as $La_{2-x}Sr_xCuO_4$. However, before the discovery of high T_c cuprates, materials such as La_2NiO_4 were of interest due to the shortness of the basal Ni–O bonds (relative to NiO) and the possibility of antiferromagnetic Ni–O–Ni interactions (28). The structures and properties of these 0201 phases are highly dependent on their oxygen contents; for example, nonstoichiometric $La_2NiO_{4+\delta}$ ($\delta \sim 0.1$) is tetragonal at ambient temperature, whereas nearly stoichiometric $La_2NiO_{4+\delta}$ ($\delta \approx 0$) is orthorhombic and displays long-range magnetic ordering (19). The presence within the $Tl(Ln_2Sr_2)Ni_2O_9$ family of the same infinite NiO_2 layers found in the 0201 nickelates suggests that the new materials may exhibit similar magnetic and electronic properties to those of the widely studied system $La_{2-x}Sr_xNiO_4$ ($0 \leq x \leq 1.67$) (2, 21, 29). $La_{2-x}Sr_xNiO_4$ undergoes a metal-insulator transition with

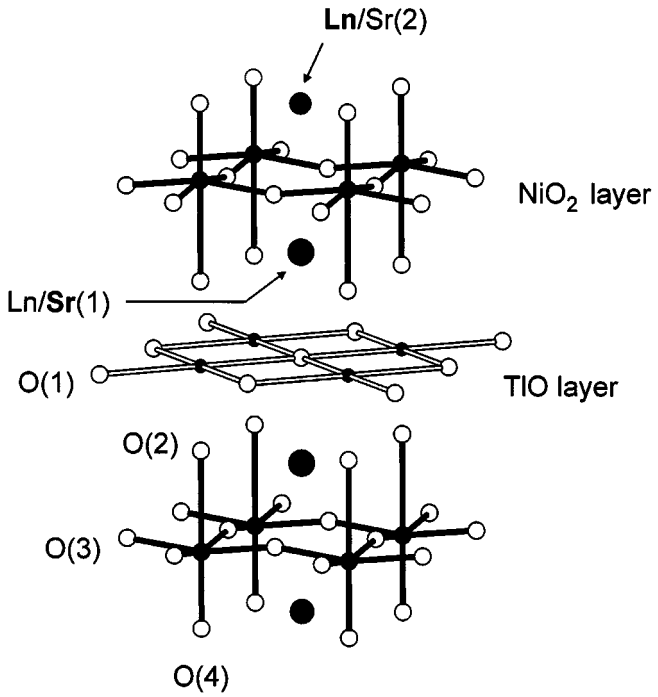

FIG. 7. Thallium–oxygen and nickel–oxygen layers present in the $Tl(Ln_2Sr_2)Ni_2O_9$ materials; cationic ordering is also shown with the preferential occupancy of the *Ln*/Sr(1) site by Sr and the *Ln*/Sr(2) site by the lanthanide.

increasing x; La_2NiO_4 is an antiferromagnetic insulator (30) but metallic behavior is observed for materials with $1.0 \leq x \leq 1.3$ (31). Takeda *et al.* (2) concluded that the structural evolution of the NiO_6 octahedron that occurs with the oxidation of the nickel ion is correlated with the changes in the physical properties of the compounds. A recent PND study has confirmed that a pronounced loss of the tetragonal distortion of the NiO_6 octahedron occurs at a doping level of $x \geq 0.6$, coincident with a sharp increase in the electrical conductivity (32). This observation is consistent with the delocalization of the e_g electrons at this composition. It is noteworthy that these structural and transport transitions occur at a nickel oxidation state of $+2.6$, very close to the nickel valence present in the $Tl(Ln_2Sr_2)Ni_2O_9$ compounds of $+2.5$. The Ni–O environments determined for the new 1201–0201 family of nickelates are clearly, therefore, of considerable interest. Table 7 compares the nickel–oxygen coordination determined for the new phases with those found in the literature on related rare earth nickel oxide phases. The compounds $La_{2-x}Sr_xNiO_4$ ($x = 0$, 0.6, 1, and 1.6) (2), $Nd_{2-x}Sr_xNiO_4$ ($x = 0.2$, 0.6, 1, and 1.2) (22), $Sm_{2-x}Sr_xNiO_4$ (20) ($x = 0.4$, 0.6, 1, and 1.2), and $GdSrNiO_{4-\delta}$ (21) have oxygen contents of 4 ± 0.05 and consequently provide a good comparison with the 1201–0201 phases, which contain stoichiometric NiO_6 octahedra. Data on $Gd_{0.33}Sr_{1.67}NiO_{4-\delta}$ (21) which exhibit an appreciable level of oxygen deficiency, i.e., $\delta = 0.3$, is also included for completeness.

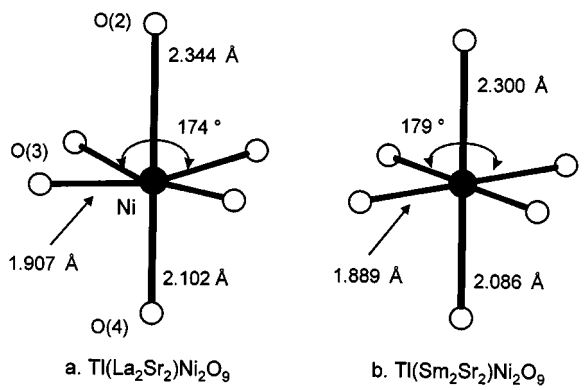

FIG. 8. The nickel–oxygen coordination present in $Tl(La_2Sr_2)Ni_2O_9$ (Fig. 8a) and $Tl(Sm_2Sr_2)Ni_2O_9$ (Fig. 8b) determined from PND data.

Table 7 reveals that the shortest Ni–O basal distances for the strontium-substituted K_2NiF_4 materials containing the larger lanthanides, e.g., La and Nd, correspond to a nickel oxidation state of ~ 2.6, approximately, the nickel valence present in the intergrowth materials. In the strontium-substituted K_2NiF_4 phases there are two competing factors which influence the a parameter (and the basal Ni–O distance), i.e., the incorporation of the larger strontium ion and the simultaneous oxidation of Ni(II) to Ni(III). These two factors produce a minimum in the basal distance when the ratio of Ni^{2+}/Ni^{3+} is close to 1. The table shows that there is good agreement between the in-plane bond lengths of the two families of compounds at this valence state; i.e., $La_{1.4}Sr_{0.6}NiO_{4.04}$ has a Ni–O distance of 1.9043(1) Å (2) and $Tl(La_2Sr_2)Ni_2O_9$ has a Ni–O bond length of 1.904(1) Å (PXD data). The results also show that the mean apical Ni–O interactions in $Tl(Ln_2Sr_2)Ni_2O_9$, Ln = La and Nd, are in line with the Ni–O(2) values determined for their K_2NiF_4 couterparts. As the rare earth ion becomes smaller, the amount of strontium substitution required to stabilize the 0201 structure becomes greater, leading to the formation of solid solutions in the range $0.4 \leq x \leq 1.6$ for $Sm_{2-x}Sr_xNiO_{4+\delta}$ (20) ($\delta \approx 0$) and $1.0 \leq x \leq 1.67$ for $Gd_{2-x}Sr_xNiO_{4-\delta}$ (21). The basal Ni–O distances of 1.891(1) and 1.881(1) Å determined for $Sm_{2-x}Sr_xNiO_4$ with $x = 0.4$ ($Ni^{2.45+}$) and 0.6 ($Ni^{2.6+}$) respectively show good agreement with the value for $Tl(Sm_2Sr_2)Ni_2O_9$. The inability to form phases with $x < 1$ for $Gd_{2-x}Sr_xNiO_{4-\delta}$ means that a comparison between $Tl(Gd_2Sr_2)Ni_2O_9$ and a K_2NiF_4 counterpart with isovalent nickel is not possible. Table 7 shows that the basal Ni–O distance determined for $Tl(Gd_2Sr_2)Ni_2O_9$ of 1.883 Å is shorter than those obtained for the oxygen-deficient Ni(III) phases $Gd_{2-x}Sr_xNiO_{4-\delta}$, and is amongst the shortest Ni–O bonds so far determined. This result suggests that the 1201–0201 structure introduces

TABLE 6
Interatomic Distances (in Å) and O(3)–Ni–O(3) Bond Angle (°) Derived from PND (e.s.d.'s Are Given in Parentheses; Final Fit Parameters Are Also Shown; * Indicates 5-K Data)

	$Tl(Ln_2Sr_2)Ni_2O_9$						
Bond	La	La*	Pr	Pr*	Nd	Nd*	Sm
Tl–O(1) × 2	2.974 − 2.223(5)	2.941–2.076(3)	2.970 − 2.186(7)	2.925 − 2.193(2)	2.947 − 2.215(8)	2.916 − 2194(3)	3.008 − 2.139(14)
Tl–O(2) × 2	2.092(2)	2.076(3)	2.092(3)	2.080(3)	2.096(3)	2.080(3)	2.106(5)
Ln(1)–O(1) × 1	2.5529(15)	2.532(3)	2.5471(19)	2.515(4)	2.5441(18)	2.514(3)	2.559(3)
Ln(1)–O(2) × 4	2.7312(5)	2.7256(8)	2.7168(6)	2.7079(8)	2.7099(6)	2.7035(8)	2.7076(10)
Ln(1)–O(3) × 4	2.6125(16)	2.610(3)	2.6045(20)	2.617(4)	2.5994(20)	2.613(3)	2.641(4)
Ln(2)–O(3) × 4	2.6098(14)	2.608(3)	2.5911(20)	2.576(3)	2.5652(18)	2.551(3)	2.520(3)
Ln(2)–O(4) × 4	2.7251(4)	2.7157(6)	2.7112(5)	2.7026(7)	2.7092(5)	2.7012(7)	2.7061(10)
Ln(2)–O(4) × 1	2.397(3)	2.386(4)	2.326(4)	2.317(5)	2.322(4)	2.318(4)	2.313(7)
Ni–O(3) × 4	1.9068(1)	1.9016(2)	1.8963(1)	1.8907(1)	1.8916(1)	1.8872(1)	1.8891(1)
Ni–O(2) × 1	2.344(2)	2.344(4)	2.322(3)	2.316(4)	2.296(3)	2.294(4)	2.300(6)
Ni–O(4) × 1	2.102(2)	2.099(4)	2.099(3)	2.088(4)	2.103(3)	2.090(4)	2.086(7)
O(3)–Ni–O(3)	174.0(1)	174.8(2)	174.9(1)	176.0(2)	175.8(2)	177.0(2)	179.2(4)
R_p (%)	3.82	4.18	4.05	4.64	4.23	3.92	4.94
R_{wp} (%)	2.35	5.39	2.91	6.17	2.67	5.04	3.03
χ^2	5.15	2.20	5.74	2.84	3.87	2.18	8.00

an extra degree of flexibility and allows the coexistence of $Ni^{2.5+}$–O_2 layers and Gd/Sr–O layers. The decrease in the basal Ni–O distance observed for $Tl(Gd_2Sr_2)Ni_2O_9$ is not accompanied by a similar decrease in the axial Ni–O interactions. The mean apical distance is ~0.2 Å longer than the equivalent distance observed for $GdSrNiO_{4-\delta}$, reflecting the presence of Ni(II) in the intergrowth phase.

Future work on the 1201–0201 series will involve varying the initial *Ln*/Sr stoichiometry and monitoring the effects on the structure and the magnetic properties of the phases. The $Tl(Ln/Sr)_4Ni_2O_9$ system may allow the formation of a wide range of Ni–O planar distances with different nickel oxidation states for the medium-sized rare earths such as Gd, depending on the lanthanide/strontium ratio. The presence of a TlO layer within the $Tl(Ln_2Sr_2)Ni_2O_9$ structure results in a lower Ni oxidation state of +2.5 compared to +3.0 for the closely related K_2NiF_4 phases with 1:1 ratios of *Ln* and Sr. Consequently, the end members of the solid solution, $TlLn_4Ni_2O_9$ and $TlSr_4Ni_2O_9$ (if they could be synthesized), would have nickel oxidation states ranging from +1.5 to +3.5, respectively, compared with Ni of +2 to +4 for the $Ln_{2-x}Sr_xNiO_4$ series. The difficulty in obtaining nickel oxidation states higher than +3 without oxygen annealing may limit the level of strontium substitution within the intergrowth structure to $Tl(LnSr_3)Ni_2O_9$. The lower limit of strontium substitution is likely to occur at $Tl(Ln_3Sr)Ni_2O_9$, i.e., Ni(II) since the introduction of Ni(I) into the structure is improbable. An experimental consideration is the use of the $Sr_2Ni_2O_5$ precursor in the synthesis of the new materials would only permit the Sr content to be increased, possibly using SrO as a source of additional Sr, and the lanthanide concentration decreased proportionally, i.e., investigations on $Tl(Ln_{2-x}Sr_{2+x})Ni_2O_9$, $x \geq 1$ only will be possible.

MAGNETIC PROPERTIES

The magnetic behaviors of $Tl(La_2Sr_2)Ni_2O_9$ and $Tl(Gd_2Sr_2)Ni_2O_9$ were measured using a vibrating sample magnetometer. The samples were cooled to 4 K in zero field and the magnetization was measured while warming to 300 K under an applied field of 300 G. The results are shown in Fig. 9; both materials exhibit paramagnetic behavior. The data for $Tl(La_2Sr_2)Ni_2O_9$ can be fitted to the Curie–Weiss equation in the region 100–280 K (see inset of Fig. 9a), yielding a $\mu_{eff} = 3.31\ \mu_B$ per nickel ion and a Weiss constant $\theta = -518.1$ K. Fitting the data obtained for $Tl(Gd_2Sr_2)Ni_2O_9$ to the Curie–Weiss law over the range 300–400 K gives a $\mu_{eff} = 6.41\ \mu_B$ and $\theta = -23.0$ K. The μ_{eff} value is much larger than that determined for $Tl(La_2Sr_2)Ni_2O_9$ due to the contribution from the paramagnetic Gd^{3+} ion and this prevents the magnetic moment of nickel being estimated accurately.

The data for $Tl(La_2Sr_2)Ni_2O_9$ indicate the presence of Ni^{2+} and high-spin Ni^{3+} rather than low spin. This result would be unusual as high-spin Ni(III) is not commonly found in such oxide materials. In addition, the apically distorted NiO_6 environment is associated with the

TABLE 7

Comparison of the Nickel–Oxygen Coordinations Present in the Tl(Ln_2 Sr_2)Ni_2O_9 Family with Those Determined for Related Rare Earth K_2NiF_4 Phases (The Approximate Nickel Oxidation State Is Also Shown; All Bond Lengths Are Calculated from PXD Data and Given in Å)

Material	Ni oxidation state	Ni–O basal	Ni–O apical
[a]La_2NiO_4	2	1.9345(1)	2.26(2)
$La_{1.4}Sr_{0.6}NiO_4$	2.6	1.9043(1)	2.11(5)
$LaSrNiO_4$	3.0	1.9129(1)	2.05(4)
$La_{0.4}Sr_{1.6}NiO_4$	3.6	1.9095(1)	1.99(3)
Tl(La_2Sr_2)Ni_2O_9	2.5	1.904(1)	2.23/2.14(3)
[b]$Nd_{1.8}Sr_{0.2}NiO_4$	2.2	1.9096(1)	2.19(6)
$Nd_{1.4}Sr_{0.6}NiO_4$	2.6	1.8862(1)	2.13(5)
$NdSrNiO_4$	3.0	1.8984(1)	2.03(4)
$Nd_{0.8}Sr_{1.2}NiO_4$	3.2	1.9002(1)	1.97(3)
Tl(Nd_2Sr_2)Ni_2O_9	2.5	1.893(1)	2.25/2.14(3)
[c]$Sm_{1.6}Sr_{0.4}NiO_4$	2.45	1.891(1)	2.161(6)
$Sm_{1.4}Sr_{0.6}NiO_4$	2.6	1.8881(1)	2.119(5)
$SmSrNiO_4$	3.0	1.892(1)	2.036(5)
$Sm_{0.8}Sr_{1.2}NiO_4$	3.2	1.896(1)	2.000(4)
Tl(Sm_2Sr_2)Ni_2O_9	2.5	1.887(1)	2.19/2.17(4)
[d]$GdSrNiO_{4-\delta}$	3.0	1.886(1)	2.055(6)
$Gd_{0.67}Sr_{1.33}NiO_{4-\delta}$	3.0	1.894(1)	2.003(5)
Tl(Gd_2Sr_2)Ni_2O_9	2.5	1.883(1)	2.30/2.14(5)

[a] Reference [2].
[b] Reference [22].
[c] Reference [20].
[d] Reference [21].

Jahn–Teller active low-spin state. However, the elongation of the NiO_6 octahedra may be a result of the bonding requirements of the surrounding La/Sr–O network rather than a consequence of Jahn–Teller effects. Below $\sim$ 50 K the data deviate from the Curie–Weiss law, possibly indicating low-temperature ordering of the nickel spins. It is feasible that this affects the reliability of the μ_{eff} value determined for Tl(La_2Sr_2)Ni_2O_9. Alternatively, the presence of a small amount of magnetically active impurity may be responsible for the larger than expected moment. This seems unlikely as the only secondary phase detected by diffraction was a small level of NiO (T_{Neel} = 523 K). Further investigation into the magnetic behavior of the material using higher temperature data, i.e., 400–600 K may clarify the spin state. A recent report of high-spin Ni^{3+} based on susceptibility and structural data in the related cation disordered $LaSrNi_{0.5}Mn_{0.5}O_{4+\delta}$ is of note (33).

Both Tl(La_2Sr_2)Ni_2O_9 and Tl(Gd_2Sr_2)Ni_2O_9 have negative Weiss constants, indicating antiferromagnetic coupling of the spins within the Ni^{2+}/Ni^{3+}–O_2 planes. The lower value determined for Tl(Gd_2Sr_2)Ni_2O_9 suggests that the presence of the paramagnetic Gd^{3+} ion either frustrates or obscures the ordering of the nickel sublattice. The absence of a T_{Neel} associated with the gadolinium ion may be attributed to the dilution of the paramagnetic moments of the Gd^{3+} ions by the diamagnetic Sr^{2+} ions as previously described (19). Studies into the magnetic properties of the whole 1201–0201 family (La, Pr, Nd, Sm, Eu, and Gd) are currently being undertaken.

CONCLUSIONS

A new family of complex nickel oxides described by the formula Tl(Ln_2Sr_2)Ni_2O_9, Ln = La, Pr, Nd, Sm, Nd, and Gd, have been synthesized and their structures determined using Rietveld analysis of powder X-ray diffraction and powder neutron diffraction data. The materials are isostructural with the superconducting cuprate phase

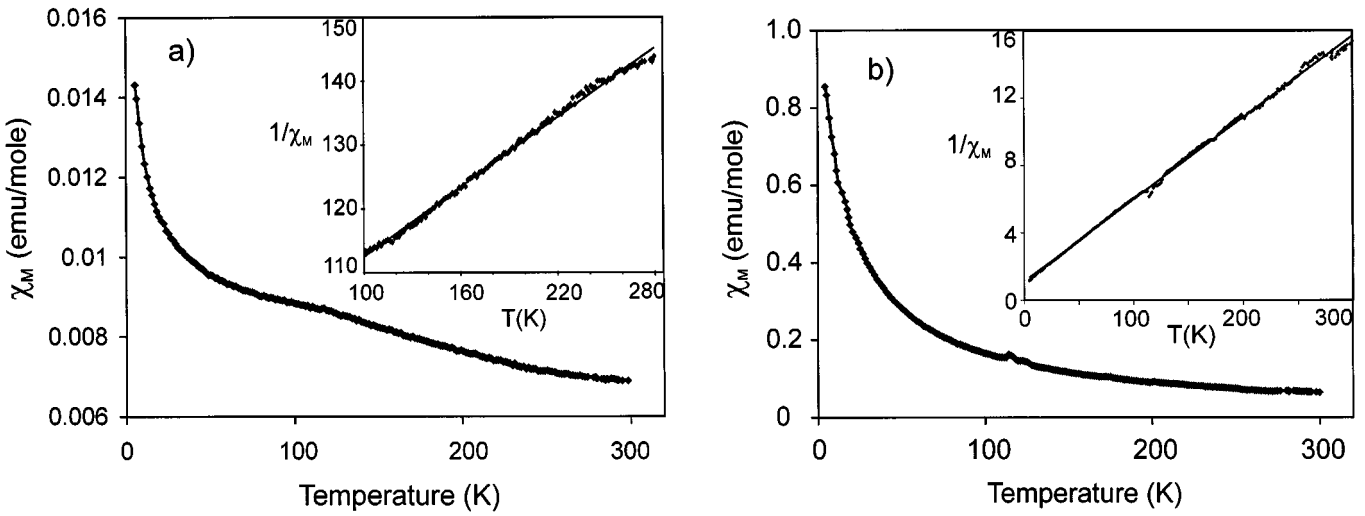

FIG. 9. Molar magnetic susceptibility χ_M (e.m.u/mol) of Tl(La_2Sr_2)Ni_2O_9 (Fig. 9a) and Tl(Gd_2Sr_2)Ni_2O_9 (Fig. 9b) over a temperature range 300–400 K. The fits to the inverse χ_M vs temperature plots are shown in the insets.

$Tl(Ba_{1.6}La_{2.4})Cu_2O_9$, adopting the tetragonal 1201–0201 intergrowth structure. The compounds exhibit the expected decrease in cell constants consistent with the lanthanide contraction. A phase transition, attributed to the lanthanide ion becoming too small to stabilize the structure, occurs at Tb. Structural analysis using PXD data reveals partial ordering of the *Ln* and Sr atoms on the two cationic sites. The segregation is attributed to the size mismatch between Ln^{3+} and Sr^{2+} and it increases as the lanthanide becomes smaller. The phases also exhibit thallium–oxygen disorder and buckling of the NiO_2 planes within the basal plane. The 1201–0201 structure allows the stabilization of short Ni–O basal distances with nickel present in a mixed valent state, similar to the important K_2NiF_4 $Ln_{2-x}Sr_xNiO_{4\pm\delta}$ series. The 1201–0201 structure, however, allows the formation of particularly short in-plane $Ni^{2.5+}$–O bonds in $Tl(Gd_2Sr_2)Ni_2O_9$ (1.883 Å) while $Gd_{1.5}Sr_{0.5}Ni^{2.5+}O_4$ cannot be synthesized. The irregular NiO_6 coordination, i.e., two Ni–O apical distances and buckled planes, present in the $Tl(Ln_2Sr_2)Ni_2O_9$ oxides are believed to be the result of the cationic ordering producing two different rock salt layers above and below the NiO_6 octahedron. The magnetic properties of two representative phases exhibit Curie–Weiss-like dependence. Investigation of the structures of $Tl(Ln_2Sr_2)Ni_2O_9$, *Ln* = La, Pr, Nd, and ^{154}Sm, by powder neutron diffraction confirmed the stoichiometric oxygen content of the materials and allowed the formal valence of nickel to be determined as $+2.5$. Analysis of the PND data also showed a decrease in the O(3)–Ni–O(3) bond angle as the lanthanide ion becomes smaller, confirming that the buckling is due to the bonding requirements of the surrounding *Ln*/Sr–O framework and not because of compressive strain on the bond.

In conclusion, the $Tl(Ln_2Sr_2)Ni_2O_9$, *Ln* = La, Pr, Nd, Sm, Nd, and Gd, family provides further illustration of the ability of nickel to adopt structural analogues of well-known copper oxide materials. The presence of elongated apex sharing NiO_6 octahedra within the compounds is of particular interest given the role played by this structural element in the widely studied 0201 nickelates. Further investigations into the evolution of structural and physical properties with variations in the lanthanide/strontium ratio are in progress.

ACKNOWLEDGMENTS

The authors acknowledge the EPSRC for providing a studentship for C.S.K, a grant in aid of this work and provision of neutron beam time. The Institute Laue Langevin for neutron beam time and technical help and Dr. P. De Groot and S. Kokkaliaris, University of Southampton, Physics Department for the collection of V.S.M. data are also acknowledged.

REFERENCES

1. J. Gopalakrishnan, G. Colsmann, and B. Reuter, *J. Solid State Chem.* **22,** 145 (1977).
2. Y. Takeda, R. Kanno, M. Sakano, O. Yamamoto, M. Takano, Y. Bando, H. Akinga, K. Takita, and J. B. Goodenough, *Mater. Res. Bull.* **25,** 293 (1990).
3. Z. Kakol, J. Spalek, and J. M. Honig, *J. Solid State Chem.* **79,** 288 (1989).
4. H. Rieck and R. Hoppe, *Z. Anorg. Allg. Chem.* **392,** 193 (1972).
5. W. Losert and R. Hoppe, *Z. Anorg. Allg. Chem.* **379,** 234 (1970).
6. M. A. G. Aranda and J. P. Attfield, *Angew. Chem. Int. Ed. Engl.* **32,** 1454 (1993).
7. R. Gottscall and R. Scollhorn, *Solid State Ionics* **59,** 93 (1993).
8. C. S. Knee and M.T . Weller, *J. Mater. Chem.* **6**(8), 1449 (1996).
9. C. S. Knee and M. T. Weller, *J. Solid State Chem.* **144,** 62 (1999).
10. E. Ohshima, M. Kikuchi, F. Izumi, K. Hiraga, T. Oku, S. Nakajima, N . Ohnishi, Y. Morii, S. Funahashi, and Y. Syono, *Physica C* **221,** 261 (1994).
11. M. A. Subramanian, *Mater. Res. Bull.* **25,** 191 (1990).
12. C. S. Knee and M. T. Weller, *J. Mater. Chem.* **8,** 2585 (1998).
13. C. Martin, A. Maignan, M. Huve, M. Hervieu, C. Michel, and B. Raveau, *Physica C* **179,** 1 (1991).
14. Y. Takeda, T. Hashino, H. Miyamoto, F. Kanamaru, S. Kume, and M. Koizumi, *J. Inorg. Nucl. Chem.* **34,** 1599 (1972).
15. E. Palleta and H. Mueller-Buschbaum, *J. Inorg. Nucl. Chem.* **30,** 1425 (1968).
16. A. C. Larson and R. B. Von Dreele, MS-H805, Los Alamos National Laboratory, Los Alamos, NM, 87545.
17. S. N. Ruddlesden and P. Popper, *Acta Crystallogr.* **11,** 54 (1958).
18. R. D. Shannon, *Acta Crystallogr. Sect. A* **32,** 751 (1976).
19. S. C. Chen, K. V. Ramanujachary, and M. Greenblatt, *J. Solid State Chem.* **105,** 444 (1993).
20. H. Lou, Y. Ge, P. Chen, M. Mei, F. Ma, and G. Lü, *J. Mater. Chem.* **7**(10), 2097 (1997).
21. M. James and J. P. Attfield, *J. Mater. Chem.* **6**(1), 57 (1996).
22. Y. Takeda, M. Hishijima, N. Imanishi, R. Kanno, and O. Yamamoto, *J. Solid State Chem.* **96,** 72 (1992).
23. M. James, J. P. Attfield, and J. Rodriguez-Carvajal, *Chem. Mater.* **7,** 1448 (1995).
24. C. Michel, E. Suard, V. Caignaert, C. Martin, A. Maignan, M. Hervieu, and B. Raveau, *Physica C* **178,** 29 (1991).
25. M. A. Subramanian, G. H. Kwei, J. B. Parise, J. A. Goldstone, and R. B. Von Dreele, *Physica C* **166,** 19 (1990).
26. P. Daniel, L. Barbey, D. Groult, N. Nguyen, G. Van Tendeloo, and B. Raveau, *Eur. J. Solid State Inorg. Chem.* t.**31,** 235 (1994).
27. L. Koester, H. Rauch, and E. Seymann, *At. Data Nucl. Data Tables* **49,** 65 (1991).
28. D. J. Buttrey, J. M. Honig, and C. N. R. Rao, *J. Solid State Chem.* **64,** 287 (1986).
29. C. N. R. Rao, P. Ganguly, K. K. Singh, and R. A. Mohan Ram, *J. Solid State Chem.* **72,** 14 (1988).
30. C. N. R. Rao, D. J. Buttrey, N. Otsuka, P. Ganguly, H. R. Harrison, C. J. Sandberg, and J. M. Honig, *J. Solid State Chem.* **51,** 266 (1984).
31. K. Sreedhar, and J. M. Honig, *J. Solid State Chem.* **111,** 147 (1994).
32. J. E. Millburn, M. A. Green, D. A. Neumann, and M. J. Rosseinsky, *J. Solid State Chem.* **145,** 401 (1999).
33. J. E. Millburn and M. J. Rosseinsky, *J. Mater. Chem.* **8**(6), 1413 (1998).